



Conversion degree and heat transfer in the cold cap and their effect on glass production rate in an electric melter

April 2023

Changing the World's Energy Future

Pavel Ferkl, Pavel Hrna, Alexander W Abboud, Donna Post Guillen, Miroslava Vernerov, Jaroslav Klouek, Mark Hall, Albert Kruger, Richard Pokorny



DISCLAIMER

This information was prepared as an account of work sponsored by an agency of the U.S. Government. Neither the U.S. Government nor any agency thereof, nor any of their employees, makes any warranty, expressed or implied, or assumes any legal liability or responsibility for the accuracy, completeness, or usefulness, of any information, apparatus, product, or process disclosed, or represents that its use would not infringe privately owned rights. References herein to any specific commercial product, process, or service by trade name, trade mark, manufacturer, or otherwise, does not necessarily constitute or imply its endorsement, recommendation, or favoring by the U.S. Government or any agency thereof. The views and opinions of authors expressed herein do not necessarily state or reflect those of the U.S. Government or any agency thereof.

Conversion degree and heat transfer in the cold cap and their effect on glass production rate in an electric melter

**Pavel Ferkl, Pavel Hrna, Alexander W Abboud, Donna Post Guillen, Miroslava
Vernerov, Jaroslav Klouek, Mark Hall, Albert Kruger, Richard Pokorny**

April 2023




**Idaho National Laboratory
Idaho Falls, Idaho 83415**

<http://www.inl.gov>

**Prepared for the
U.S. Department of Energy
Under DOE Idaho Operations Office
Contract DE-AC07-05ID14517**

RESEARCH ARTICLE

Conversion degree and heat transfer in the cold cap and their effect on glass production rate in an electric melter

Pavel Ferkl¹  | Pavel Hrma² | Alexander Abboud³  | Donna Post Guillen³  |
Miroslava Vernerová^{4,5} | Jaroslav Kloužek^{4,5}  | Mark Hall¹ | Albert A. Kruger⁶ |
Richard Pokorný^{4,5} 

¹Pacific Northwest National Laboratory, Richland, Washington, USA

²AttainX, Support Services Contractor to the Office of River Protection, U.S. Department of Energy, Richland, Washington, USA

³Idaho National Laboratory, 995 University Blvd., Idaho Falls, Idaho, USA

⁴Laboratory of Inorganic Materials, University of Chemistry and Technology Prague, Prague, Czech Republic

⁵Institute of Rock Structure and Mechanics, Czech Academy of Sciences, Prague, Czech Republic

⁶U.S. Department of Energy, Office of River Protection, Richland, Washington, USA

Correspondence

Pavel Ferkl, Pacific Northwest National Laboratory, Richland, WA 99354, USA.
Email: pavel.ferkl@pnnl.gov

Funding information

Czech Ministry of Education, Grant/Award Number: LTAUSA18075; U.S. Department of Energy Idaho, Grant/Award Number: DE-AC07-05ID14517; U.S. Department of Energy and the Nuclear Science, Grant/Award Number: DE-AC07-05ID14517

Abstract

A predictive model of melt rate in waste glass vitrification operations is needed to inform melter operations during normal and off-normal operations. This paper describes the development of a model of the cold cap (the reacting melter feed floating on molten glass in a glass melter) that couples heat transfer with the feed-to-glass conversion kinetics. The model was applied to four melter feeds designed for high-level and low-activity nuclear waste feeds using the material properties, either measured or estimated, to obtain temperature and conversion distribution within the cold cap. The cold cap model, when coupled with a computational fluid dynamics model of a Joule-heated glass melter, allows the prediction of the glass production rate and power consumption. The results show reasonable agreement with the melting rates measured during pilot-scale melter tests.

KEYWORDS

batch reactions, heat transfer, modeling, nuclear waste, reaction kinetics

1 | INTRODUCTION

Common mathematical representations of glass melters compute temperature and velocity fields in the molten

glass and the furnace atmosphere to optimize energy consumption and conditions for producing a homogeneous glass using production rate as an input and rather than as a result of the simulation.^{1–8} This can only be achieved if the

This is an open access article under the terms of the [Creative Commons Attribution-NonCommercial](https://creativecommons.org/licenses/by-nc/4.0/) License, which permits use, distribution and reproduction in any medium, provided the original work is properly cited and is not used for commercial purposes.

© 2022 The American Ceramic Society and Wiley Periodicals LLC.

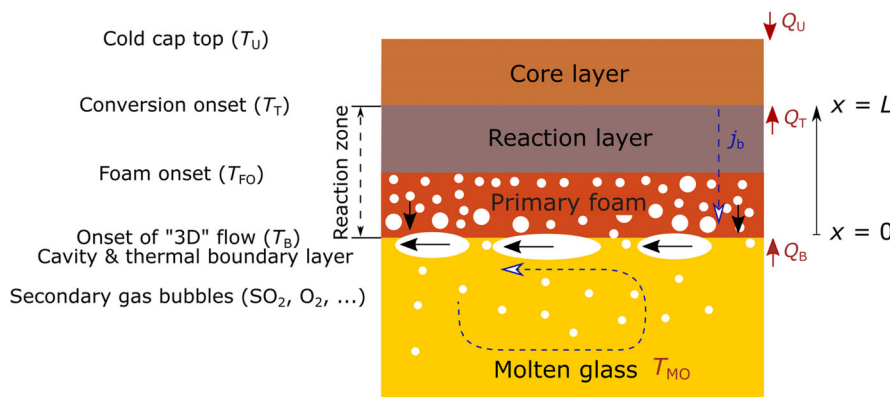


FIGURE 1 Simplified cold cap structure used for mathematical modeling, where L is the thickness of the reaction zone (including primary foam); j_b is the mass flux of condensed materials; Q_B , Q_T , and Q_U are the heat fluxes to the bottom of the cold cap, and from the reaction layer to the core layer, and to the top of the cold cap, respectively; T_U , T_T , T_{FO} , and T_B are the temperatures at the top of the cold cap, the top of the reaction layer, the foam onset, and the bottom of the cold cap, respectively; T_{MO} is the melter operating temperature.

cold cap, a mass of reacting material that floats on the glass melt surface, is realistically described by a mathematical model that uses the reaction kinetics to describe the spatial distribution of feed-to-glass conversion inside the cold cap. The feed-to-glass conversion process consists of multiple interdependent, both simultaneous and sequential, reactions that progress within the cold cap over the distance of a few centimeters and a temperature span of almost a thousand kelvin.^{9–13} As a detailed description of such complex processes inside the cold cap is impractical, it is necessary for cold cap models to make simplifying assumptions.^{9,14–17}

In this study, we estimate the rate of melting at the cold cap bottom, which when integrated over the cold cap bottom area, governs the glass production rate of an electric melter. The methodology is also applicable to a portion of the glass production rate in a combustion-fired glass furnace as heat from the melt is delivered to reacting materials by the same mechanism. Figure 1 schematically depicts the structure of the cold cap in an electric melter, illustrating a section through the cold cap sufficiently distant from vent holes, cracks, and rims, so that edge effects are negligible. Within the cold cap, the condensed material (a mixture of solid and liquid components of the reacting melter feed) moves downward, undergoing multiple reactions and phase transitions as its temperature increases.

The cold cap structure consists of three layers: the core layer, the reaction layer, and the primary foam layer. Major conversion reactions start at the conversion onset temperature, T_T , which separates the core layer from the reaction layer.¹⁶ The core layer thickness varies in response to fluctuating material supply from above.^{16,18} The reaction zone represented by the cold cap model consists of the reaction layer where most of the feed-to-glass conversion occurs and the foam layer that separates the cold cap from the glass melt below.

Section 2 outlines the mathematical model. Neglecting the edge effects, the heat and mass transfer is approximated as one-dimensional within the cold cap. The feed-to-glass conversion degree is defined by the silica dissolution extent.¹⁹ To facilitate easy implementation into a CFD melter model, the formulation of a surrogate cold cap model is presented.

Section 3 lists data used to estimate properties of the cold cap: the conversion enthalpy, effective thermal conductivity, effective heat capacity, mass density, and parameters of the silica dissolution kinetics.

In Section 4, the cold cap model is applied to four simulant melter feeds, Al-19, NG-Fe2, AN-105, and AZ-102, characterized in a previous communication.¹⁹ These feeds represent specific examples formulated for high-level (HLW) and low-activity (LAW) radioactive wastes to be vitrified in slurry-fed melters at the Waste Treatment and Immobilization Plant at the Hanford Site in the U.S. State of Washington.²⁰ The cold cap model is implemented as a boundary condition in the three-dimensional CFD model of a research-scale melter. The profiles of temperature and conversion degree are displayed as functions of the vertical position in the cold cap. The glass production rate is then expressed as the average over the cold cap surface area. Estimated glass production rate and power delivery to the melter for these four feeds are compared with reported data.

2 | COLD CAP MODEL

2.1 | Heat transfer equation

To design a simple, yet realistic, cold cap model, the following assumptions are used. First, we neglect potential horizontal flow of molten salts, which, if it occurs,

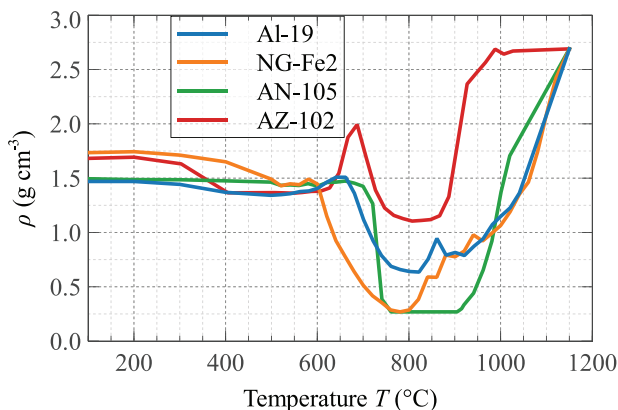


FIGURE 2 Cold cap density as a function of temperature estimated from the feed expansion test (FET) data¹⁹

may cause processing problems.²¹ Further, we assume that feed components move with the same velocity, $v(x)$, at any point x within the cold cap, allowing the condensed phases to be treated as a single material. Thus, phenomena such as molten salt drainage²² are ruled out. Next, we assume that the gas phase and condensed phase are in local thermal equilibrium,¹¹ that is, the gas temperature is the same as the condensed phase temperature at any point x within the cold cap. Consequently, hot gases produced at a lower point in the cold cap exchange heat with the condensed phase as they rise through open pores. Finally, the conversion is tracked by the kinetic model described in Section 2.2.

The cold cap model, presented in the following, determines the nonlinear temperature history of the feed material within the cold cap and its effect on the cold cap bottom temperature, T_B , through which the cold cap model is, as a boundary condition, coupled with the CFD model of the whole melter. The cold cap model couples the feed-to-glass conversion kinetics with the heat transfer in a waste glass melter operating at steady state.

The temperature and velocity fields are three-dimensional in the glass melt and the furnace atmosphere (melter plenum). Inside the cold cap, the horizontal heat and mass fluxes are negligible; thus, the velocity and temperature fields are essentially one-dimensional,^{9,16} and the motion of material within the cold cap is predominantly vertical. The energy balance is represented by the following one-dimensional equation:

$$(j_b c_{p,b} - j_g c_{p,g}) \frac{dT}{dx} = \frac{d}{dx} \left(\lambda^{\text{eff}} \frac{dT}{dx} \right) - \rho \Delta H \frac{d\alpha}{dt} \quad (1)$$

where j is the mass flux, c_p is the heat capacity, λ^{eff} is the effective heat conductivity, which accounts for both conduction and radiation, x is the spatial position on the

vertical axis directed upward with origin at the cold cap bottom, ρ is the density, ΔH is the feed-to-glass conversion enthalpy, α is the conversion degree of gas-evolving reactions, and the subscripts b and g denote the condensed phase and the gas phase, respectively.^{9,11,15}

Substitution of $\frac{d\alpha}{dt} = v \frac{d\alpha}{dT} \frac{dT}{dx}$ to Equation (1), leads to a convenient form

$$(j_b c_{p,b}^{\text{eff}} - j_g c_{p,g}) \frac{dT}{dx} = \frac{d}{dx} \left(\lambda^{\text{eff}} \frac{dT}{dx} \right) \quad (2)$$

where $c_{p,b}^{\text{eff}} = c_{p,b} + \Delta H \frac{d\alpha}{dT}$ is the effective heat capacity that includes both reaction and sensible heat.

In Equation (2), the mass flux of the gas phase is $j_g = \alpha(j_f - j)$, where j_f is the mass flux of the dry feed entering the cold cap, and j is the mass flux of the non-volatile portion of the feed. The condensed phase mass flux is $j_b = j_f - (j_f - j)\alpha$; thus, $\alpha = (j_f - j_b)/(j_f - j)$. The nonvolatile portion of the feed, j , equals the glass production rate (the melting rate) per area and is related to the conversion enthalpy as

$$j = (Q_B + Q_U)/\Delta H \quad (3)$$

where Q_U and Q_B are the heat fluxes delivered to the cold cap top and bottom (Figure 1). The difference $j_f - j$ equals the gas production rate per area. Although j is independent of temperature and vertical position, it depends on the horizontal position in the cold cap. The fluxes j_b and j_g depend on temperature and thus on vertical position in the cold cap through α .

2.2 | Conversion kinetics

In this work, we consider two conversion degrees—conversion degree of gas-evolving reactions, α , based on thermogravimetric analysis data²³ and the conversion degree identified as the dissolution extent (undissolved silica fraction), f , based on X-ray diffraction (XRD) data.²⁴ The conversion kinetics model is developed for the silica dissolution¹⁹ and serves to define boundary between the cold cap and the melt (see Section 2.3). The conversion rate is represented by a series of the Šesták–Berggren equations^{25,26}

$$\frac{df_i}{dt} = A_i f_i^{m_i} (1 - f_i)^{n_i} \exp \left(-\frac{E_i}{RT} \right) \quad (4)$$

where f_i is the i th subprocess conversion degree, t is the time, R is the universal gas constant, and A_i , E_i , m_i , and n_i are the i th subprocess adjustable parameters. The overall

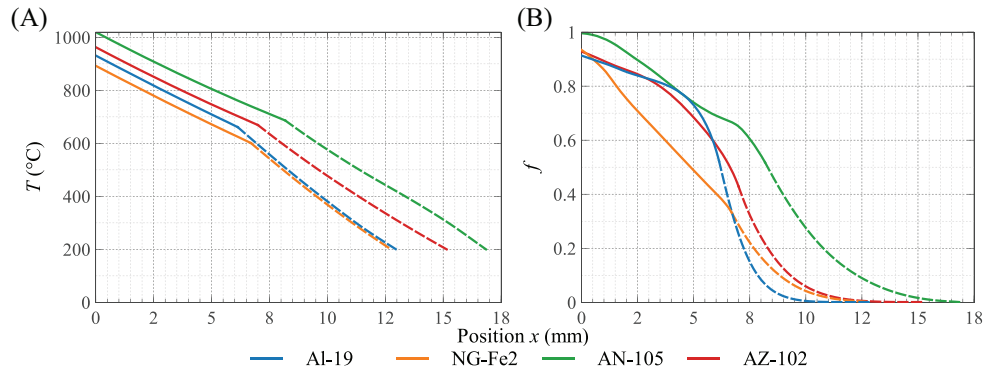


FIGURE 3 Profiles of (A) temperature and (B) fraction of dissolved silica in the cold cap for the four feeds under study; $Q_U = 6 \text{ kW m}^{-2}$, $Q_B = 60 \text{ kW m}^{-2}$, and $T_T = 200^\circ\text{C}$. The dashed lines indicate the reaction layer below T_{FO} . The estimated cold cap bottom temperature is at $x = 0$. (x increases upward through the cold cap.)

conversion rate is

$$\frac{df}{dt} = \sum_{i=1}^N c_i \frac{df_i}{dt} \quad (5)$$

where c_i is an adjustable parameter, and N is the number of terms necessary to fit the silica dissolution data.

The solution of Equation (2) is the temperature profile within the cold cap. Thus, to couple conversion kinetics with Equation (2), the temporal function $f = f(t)$ must be transformed to the spatial distribution function $f = f(x)$:

$$\frac{df}{dx} = -\frac{\rho}{j_b} \frac{df}{dt} \quad (6)$$

Note that in Equation (6), ρ , j_b , and df/dt depend on temperature and, thus, on vertical position in the cold cap.

Experimental studies performed for four feeds show that the feed-to-glass conversion for feeds NG-Fe2 and AN-105 covering the temperature interval from 300 to 1100°C and the heating rate from 2 to 30 K min^{-1} can be described as a single subprocess, that is, i can be dropped from Equation (4). However, two subprocesses are needed for feeds Al-19 and AZ-102 ($i \equiv 1, 2$).¹⁹

2.3 | Boundary conditions

Equations (2) and (6) constitute a system of coupled differential equations that would typically require three boundary conditions:

$$T|_{x=L} = T_T \quad (7)$$

$$-\lambda^{\text{eff}} \frac{dT}{dx} \Big|_{x=0} = Q_B \quad (8)$$

$$f|_{x=0} = f_B \quad (9)$$

As the thickness of the reaction layer, L , is unknown, one additional condition is needed:

$$-\lambda^{\text{eff}} \frac{dT}{dx} \Big|_{x=L} = Q_T = Q_U + j_b \int_{T_U}^{T_T} c_{p,b}^{\text{eff}} dT \quad (10)$$

The glass production rate is linked to the heat fluxes Q_U and Q_B through the overall heat balance of the cold cap given by Equation (3).

2.4 | CFD melter model

The key parts of the melter relevant to this discussion are the refractory-lined walls, melt pool, cold cap, and plenum. The CFD model computes temperature, velocity, and electric fields using the transport equations for mass, momentum, and thermal and electric energy:

$$\nabla \cdot (\rho \mathbf{v}) = 0 \quad (11)$$

$$\rho \frac{D\mathbf{v}}{Dt} = -\nabla p - \nabla \cdot \boldsymbol{\tau} + \mathbf{F}_b \quad (12)$$

$$\rho c_p \frac{DT}{Dt} = -\nabla \cdot \mathbf{q} - \nabla \cdot \mathbf{q}_r - (\boldsymbol{\tau} : \nabla \mathbf{v}) + Q_V + \sigma \nabla \phi \cdot \nabla \phi \quad (13)$$

$$\nabla \cdot (\sigma \nabla \phi) = 0 \quad (14)$$

where \mathbf{v} is the velocity vector, p is the pressure, $\boldsymbol{\tau}$ is the viscous stress tensor, \mathbf{F}_b is the body force accounting for buoyancy and momentum source by forced bubbling,³ \mathbf{q} is the conductive heat flux, \mathbf{q}_r is the radiative heat flux, Q_V is the heat-sink term accounting for atmosphere cooling due to air in-leakage, σ is the electrical conductivity, and ϕ is the electric potential.

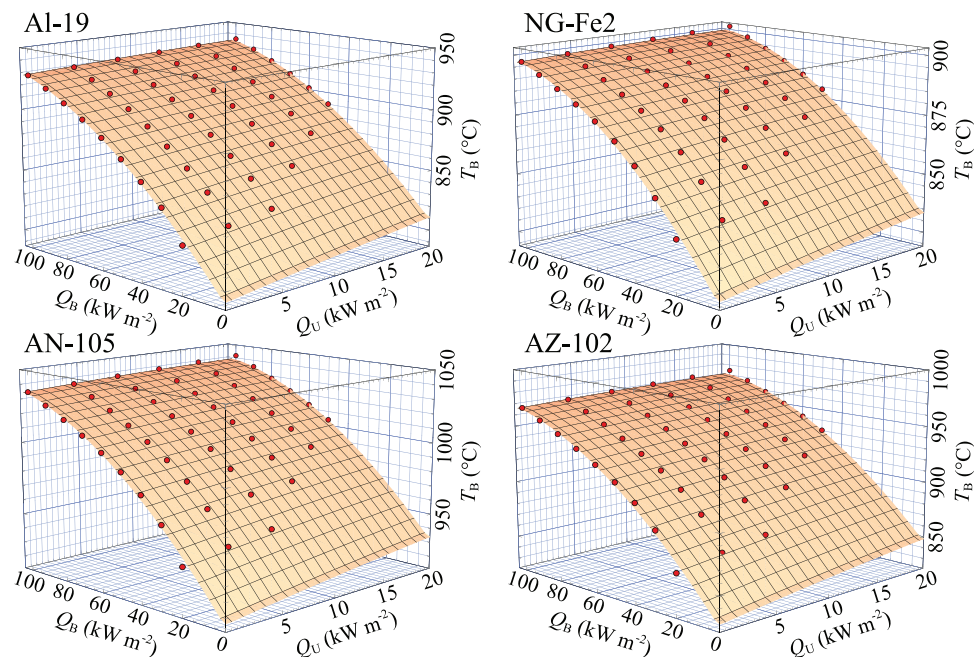


FIGURE 4 Temperature of the cold cap bottom, T_B , as a function of Q_B and Q_U . The red dots show the T_B estimated by the cold cap model. The surfaces display the $T_B(Q_B, Q_U)$ second-order polynomial, Equation (5).

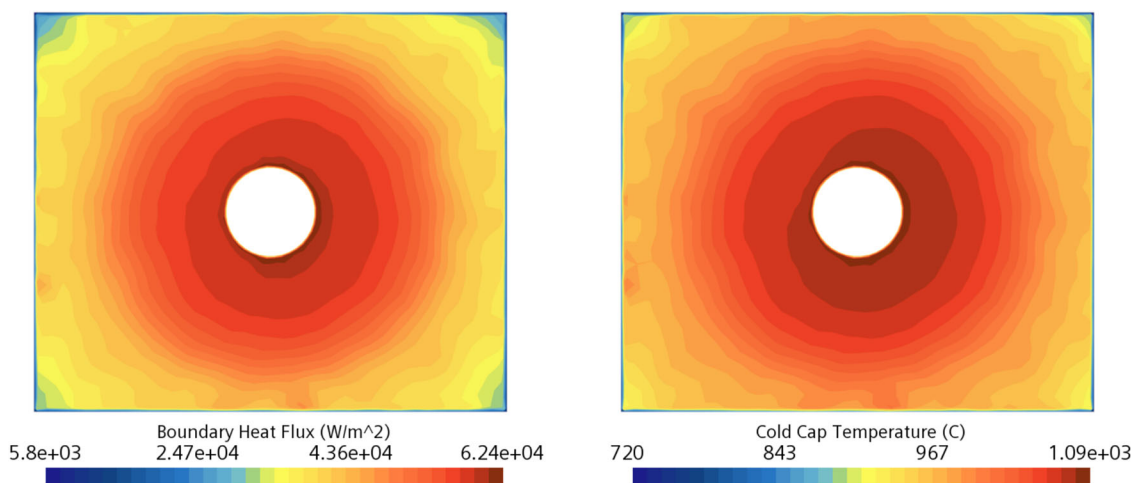


FIGURE 5 Spatial distribution of (left) heat flux and (right) temperature at the bottom of the Al-19 feed cold cap

Pressure–velocity coupling is solved using the Rhie–Chow implementation in the SIMPLE algorithm.²⁷ Discrete ordinates method was used for thermal radiation.²⁸ The volume of fluid method was used to track the melt–atmosphere interface.²⁹ Simulations with resolved bubbling were performed to determine the buoyancy momentum source³⁰ and volume fraction of air bubbles that build up underneath the cold cap, approximately $\varepsilon = 0.75$.³¹ To account for the effect of these bubbles on the heat transfer to the cold cap, the thermal conductivity below the cold cap was calculated as $\lambda = \varepsilon\lambda_a + (1 - \varepsilon)\lambda_g$, where λ_a and λ_g are the thermal conductivities of air and glass, respectively.

The values of electric potential on the electrodes are specified such that the average temperature in the bulk melt oscillates around 1150°C. Heat conduction through the refractory walls to the ambient environments was approximated using standard Nusselt number correlations. Details about cold cap boundary conditions can be found in Section 2.5.

The model was implemented in the STAR-CCM+ computational fluid dynamics software.³² It required 30 000 iterations to reach steady state. Further details on model implementation can be found in Refs.^{30,33,34} The local melting rate was estimated using Equation (3), which,

when averaged over cold cap surface, provides the glass production rate.

2.5 | Implementation of cold cap model into CFD melter model

The CFD model approximates the cold cap as a solid structure with temperature boundary conditions for its top and bottom surfaces and conjugates heat transfer on the sides and vent hole.³⁵ As the top surface is mostly covered by boiling slurry, the top temperature $T_U = 100^\circ\text{C}$. The conversion kinetics within the cold cap depends on the heating rate within the cold cap and, thus, on the heat fluxes from above Q_U and below Q_B to the cold cap. This interdependence between T_B , Q_U , and Q_B links feed composition and melter operating conditions with the rate of melting,^{36–38} affecting the driving force for heat transfer from the melt into the cold cap.^{37,38}

Directly implementing the full mathematical model of the cold cap into the CFD melter model would be computationally prohibitive because it would entail solving coupled differential equations at each cold cap boundary cell face at each time step. The process was simplified by taking advantage of Equations (2)–(10), which determine the temperature and conversion degree profiles, and hence the T_B values, as functions of the heat fluxes Q_U and Q_B , thus creating a surrogate cold cap model. With enough iterations to reach a steady state, the surrogate model provides the values of T_B , Q_U , and Q_B , where Q_U and Q_B are calculated from the temperature gradients at cold cap boundaries. As Q_U and Q_B depend on the horizontal position in the CFD model, so does the T_B .

3 | MATERIAL PROPERTIES

The incorporation of silica into glass-forming melt involves multiple processes, such as reactions with molten salts and physical dissolution in the glass-forming melt, each of which can be represented by a kinetic model. However, this was not necessary because fitting Equations (4)–(6) to XRD data revealed that two subprocesses sufficed for Al-19 and AZ-102 feeds, representing the initial reaction-controlled stage and the later diffusion-controlled stage with two sets of four adjustable parameters A_i , E_i , m_i , and n_i . XRD data of NG-Fe2 and AN-105 feeds allowed fitting Equations (4)–(6) as a single undifferentiated process.¹⁹ Table 1 lists the adjustable parameters of the kinetic model and the associated fraction of dissolved silica at the cold cap bottom, f_B .¹⁹

Table 1 also lists the total conversion enthalpy, which is a sum of the water evaporation heat, the feed reaction

TABLE 1 Fitted parameters of Equations (4)–(6)¹⁹ and other material properties^{19,36,38,42–45}

	HLW		LAW	
	Al-19	NG-Fe2	AN-105	AZ-102
c_1	.727	1.0	1.0	.790
A_1 (s^{-1})	9.51×10^{16}	3.67×10^{22}	1.02×10^{10}	1.38×10^{19}
E_1 (J mol^{-1})	3.44×10^6	5.05×10^6	2.46×10^6	4.06×10^6
m_1	−2.75	−10.9	−4.66	−5.41
n_1	1.58	2.79	1.69	2.07
c_2	0.273	0.0	0.0	0.210
A_2 (s^{-1})	1.88×10^{10}	–	–	1.18×10^8
E_2 (J mol^{-1})	3.00×10^6	–	–	2.55×10^6
m_2	−4.35	–	–	−2.44
n_2	1.68	–	–	1.39
f_B	0.913	0.934	0.999	0.928
ΔH (J g^{-1})	5919	5076	2737	3216
ρ_{1150} (kg m^{-3})	2163	2430	2485	2485
η_{1150} (Pa s)	3.33	3.04	5.20	4.20
σ_{1150} (S m^{-1})	27	33	40	20
$c_{p,1150}$ ($\text{J kg}^{-1} \text{K}^{-1}$)	1536	1730	1276	1276
λ_{1150} ($\text{W m}^{-1} \text{K}^{-1}$)	1.8	1.3	1.6	1.6

Abbreviations: HLW, high-level wastes; LAW, low-activity wastes.

heat, and the sensible heat. The water evaporation heat was calculated from the water content and specific heat of water vaporization. The reaction and sensible heat were jointly determined by the differential scanning calorimetry (DSC). The higher conversion enthalpy of HLW feeds is caused by their higher content of water and lower content of organics^{36,38}; because of the exothermal reaction of sucrose with nitrate, the reaction heat is negative for the LAW AN-105 feed.³⁶

The feed expansion test data¹⁹ are used to determine the cold cap density as a function of temperature, shown in Figure 2. For the effective heat conductivity, λ^{eff} , we used $0.7 \text{ W m}^{-1} \text{K}^{-1}$ for the open-porosity layer^{39,40} and $1.3 \text{ W m}^{-1} \text{K}^{-1}$ for the primary foam layer.⁴¹ Temperature-dependent density, viscosity, electrical conductivity, heat capacity, and thermal conductivity of glass melt are listed in Table 1 at 1150°C are taken from Refs.^{42–45}

4 | RESULTS

4.1 | Cold cap profiles

Figure 3 shows temperature and conversion degree (as the dissolved silica fraction) profiles in the cold cap for representative values of $Q_U = 6 \text{ kW m}^{-2}$, $Q_B = 60 \text{ kW m}^{-2}$, $T_U = 100^\circ\text{C}$, and $T_T = 200^\circ\text{C}$ (note that in the coupled cold cap-CFD model, neither Q_U nor Q_B are known a priori; both are obtained, together with glass production

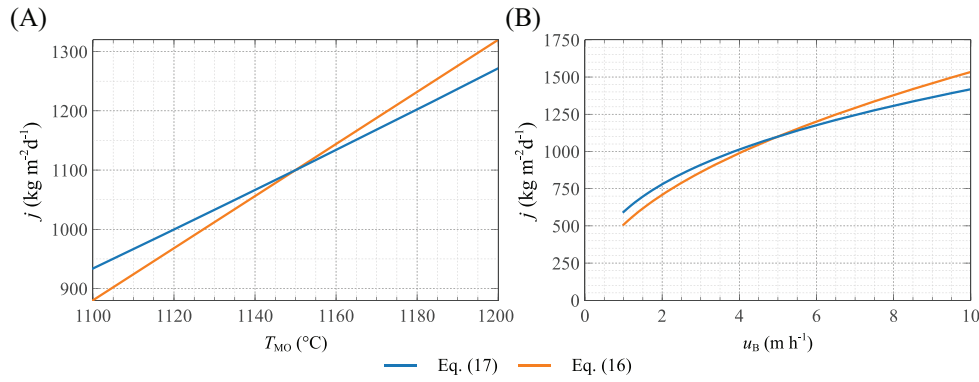


FIGURE 6 Dependence of melting rate of Al-19 feed on a changing (A) melter operating temperature and (B) bubbling rate. The value of T_B was either changing in response to changing heat flux at different operating conditions (Equation (17) with $p_B = 9.51 \times 10^{-3} \text{ K W}^{-1} \text{ m}^2$, blue lines) or retained a constant initial value (Equation 16, orange lines).

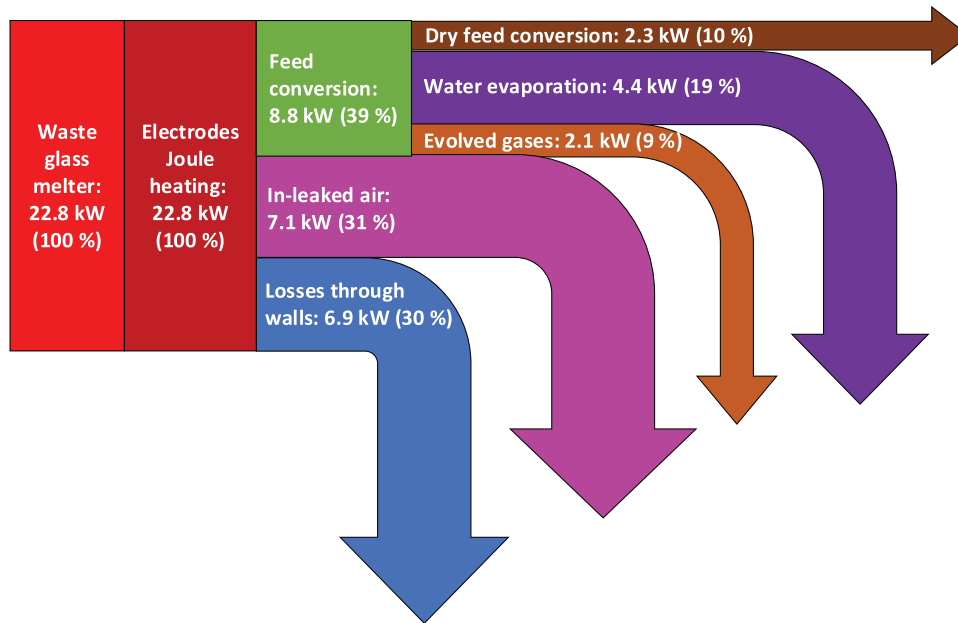


FIGURE 7 Distribution of power consumption for AN-105 waste feed in DM100 melter

rate, as the principal simulation results). As Figure 3A shows, in the 5–9 mm thick open-porosity reaction layer (dashed lines), the temperature increased from T_T to T_{FO} (600–670°C); in the 6–9 mm thick foam layer (solid lines), the temperature increases from T_{FO} to T_B (900–1010°C). In each layer, the temperature increased nearly linearly; as λ^{eff} changed from $0.7 \text{ W m}^{-1} \text{ K}^{-1}$ at $T < T_{FO}$ to $1.3 \text{ W m}^{-1} \text{ K}^{-1}$ at $T > T_{FO}$ (Section 3), the slope of the temperature profile dropped from ~ 60 to $\sim 50 \text{ K mm}^{-1}$.

As Figure 3B shows, silica starts to dissolve in the reaction layer when the temperature increases above T_T and continues to dissolve in the primary foam; a small residual fraction, $f_B = f(0) < 1$ (see Equation 9 and Table 1), drains from the cold cap into the melt below.

4.2 | Interface between cold cap model and CFD model

The system of Equations (2)–(10) with $T_T = 200^\circ\text{C}$, $T_U = 100^\circ\text{C}$, and the feed-specific parameters f_B , $c_{p,b}^{\text{eff}}$, λ^{eff} , and ρ for each feed and a set of 48 (Q_U , Q_B) pairs, where $Q_U \in (0, 4, \dots, 16, 20) \text{ kW m}^{-2}$ and $Q_B \in (20, 30, \dots, 90, 100) \text{ kW m}^{-2}$, to obtain 48 values of $T_B = F(Q_B, Q_U)$ displayed as red dots in Figure 4. Then, this function is approximated by a second-order polynomial

$$T_B = p_0 + p_U Q_U + p_B Q_B + p_{UU} Q_U^2 + p_{UB} Q_U Q_B + p_{BB} Q_B^2 \quad (15)$$

TABLE 2 Polynomial coefficients of the reduced cold cap model, Equation (15), and coefficient of determination, R^2

	HLW	NG-Fe2	LAW	AZ-102
	Al-19		AN-105	
p_0 (K)	9.04×10^2	1.03×10^3	1.09×10^3	9.30×10^2
p_U (K W ⁻¹ m ²)	4.07×10^{-3}	2.04×10^{-3}	3.58×10^{-3}	3.22×10^{-3}
p_B (K W ⁻¹ m ²)	9.51×10^{-3}	4.35×10^{-3}	8.44×10^{-3}	9.44×10^{-3}
p_{UU} (K W ⁻² m ⁴)	-8.08×10^{-8}	-3.39×10^{-8}	-7.91×10^{-8}	-7.85×10^{-8}
p_{UB} (K W ⁻² m ⁴)	-5.52×10^{-8}	-2.62×10^{-8}	-4.43×10^{-8}	-3.72×10^{-8}
p_{BB} (K W ⁻² m ⁴)	-3.08×10^{-8}	-1.72×10^{-8}	-4.65×10^{-8}	-2.41×10^{-8}
R^2	0.991	0.995	0.993	0.999

Abbreviations: HLW, high-level wastes; LAW, low-activity wastes.

where p_0 , p_i , and p_{ij} are feed-specific coefficients that depend on the feed properties $c_{p,b}^{\text{eff}}$, $\lambda_{p,b}^{\text{eff}}$, ρ , and the kinetic parameters (listed in Table 2). The orange surfaces in Figure 4 represent the polynomial functions. Equation (15), a third-type boundary condition (also known as the Robin boundary condition),⁴⁶ in which both the quantity and its derivative at the boundary are specified, is a surrogate model for the complete cold cap model. It is implemented using an iterative procedure outlined in Section 2.5.

As Figure 4 shows, T_B increases mostly with Q_B and somewhat with Q_U . In Joule-heated melters, typically about 90% of the heat is delivered to the cold cap from the melt below ($Q_B \approx 9Q_U$).¹¹ This result agrees with the general kinetics of thermally activated processes—with increased heat flux to the cold cap, the average rate of heating in the feed increases, shifting the conversion kinetics (represented here by the dissolution of silica) to higher temperatures, thus increasing the temperature at the cold cap bottom, T_B .

4.3 | Glass production rate

The coupled cold cap–CFD model is used to simulate waste glass melting in DM100 pilot-scale melters operated at Vitreous State Laboratory (VSL) at the Catholic University of America. In experiments, simulant wastes feeds were vitrified in two melters of a similar geometry and 0.108-m² melt surface area: HLW in DM100-BL melter with two sets of electrodes and LAW in DM100-WV melter with one set of electrodes.⁴² The melter operating conditions are summarized in Table 3.

Figure 5 shows the spatial distribution of heat flux and temperature at the bottom of the cold cap. Faster melt circulation near the vent hole leads to enhanced heat transfer in the cold cap vicinity in response to which the conversion process shifts to higher temperatures.

The steady-state local heat fluxes to the cold cap are averaged over the cold cap bottom surface to obtain the total heat fluxes to cold cap top and bottom surfaces, Q_U

TABLE 3 Melter operating conditions

	HLW	NG-Fe2	LAW	AZ-102
	Al-19		AN-105	
Reference	42	43	44	45
Melt pool temperature (°C)	1150	1150	1150	1150
Bubbling rate (l min ⁻¹)	9.0	8.9	8.6	9.2
Voltage (V)	41.5	44.4	37.5	65.8

Abbreviations: HLW, high-level wastes; LAW, low-activity wastes.

TABLE 4 Glass production rate (kg m⁻² day⁻¹)

	HLW	NG-Fe2	LAW	AZ-102
	Al-19		AN-105	
Measured	950	1650	1965	1997
Estimated, CFD	995	1880	1802	1445
Estimated, MRC	910	1760	1745	2605

Abbreviation: HLW, high-level wastes; LAW, low-activity wastes; MRC, melting rate correlation.

and Q_B , and then, by Equation (3), the glass production rate per unit surface area. Table 4 compares the results with the time-averaged glass production rates measured at VSL with the melting rate correlation (MRC) and CFD estimates.³⁸

The MRC estimate is based on the following equation³³:

$$j = \frac{Q}{\Delta H} = \xi_1 \left(\frac{hu_B \rho}{\eta} \right)^\gamma \frac{T_{MO} - T_B}{\Delta H} = \xi_1 Re^\gamma \frac{T_{MO} - T_B}{\Delta H} \quad (16)$$

where h is the melt pool depth, u_B is the (forced convection inducing) bubbling rate (volumetric flow rate per melt area), η is the melt viscosity, T_{MO} is the melter operating temperature, and ξ_1 and γ are fitting parameters. The ξ_1 and γ values were obtained by fitting Equation (16) to glass production rate data reported for DM100 melters: $\xi_1 = 336.7 \text{ W m}^{-1} \text{ K}^{-1}$, $\gamma = 0.479$ for HLW and $\xi_1 = 459.3 \text{ W m}^{-1} \text{ K}^{-1}$, $\gamma = 0.327$ for LAW glasses.³⁶ Equation (16) represents a relatively narrow range of data for a melter stirred by forced convection air bubbling. The

situation where $j \rightarrow 0$ as $Re \rightarrow 0$ is caused by ignoring buoyancy, which sets in when melt stirring stops.

For both the CFD calculations and MRC estimate, the agreement with reported values is better for HLW glasses than for LAW glasses; the slightly larger error for anomalous behavior for AZ-102 melter feed could be connected to its unusual foaming behavior—relatively small maximum foam volume but considerable gas evolution to high temperature.^{36,45}

As stated in Section 2.5 and shown in Section 4.2, the cold cap bottom temperature is a function of the heat flow into the cold cap. Assuming that $Q_U \ll Q_B$, hence, $Q \approx Q_B$, and neglecting second-order terms, Equation (15) reduces to $T_B = p_0 + p_B Q$. By Equation (1), $j = Q/\Delta H$. Thus, $T_B = p_0 + p_B j \Delta H$. Using this equation, Equation (16) can be rearranged as⁴⁷

$$j = \frac{T_{MO} - p_0}{\Delta H (\xi_1^{-1} Re^{-\gamma} + p_B)} \quad (17)$$

The coefficient p_B expresses the effect of the feed-to-glass conversion kinetics on the cold cap bottom temperature. As Table 2 indicates, its value is positive. Hence, T_B increases as j increases. The melting rate can be increased by increasing the melter operating temperature or the rate of bubbling. But these measures also affect T_B , which results in a smaller increase in j than one would expect providing that T_B were not affected. This is illustrated in Figure 6. Indeed, by Equation (17), the derivatives dj/dT_{MO} and dj/du_B decrease with increasing p_B .

4.4 | Macroscopic balance of the melter

The power consumption by the melter, P , which is controlled to keep a constant melter operating temperature, converts the slurry feed charged to the melter to glass (P_c), compensates for heat losses through the walls (P_w), and heats the injected (bubbling) and in-leaked air (P_a):

$$P = P_c + P_w + P_a \quad (18)$$

Table 5 lists the measured and calculated power consumption as well as heat losses calculated by the CFD model and estimated based on measured melting rate and feed properties. The calculated power consumption reasonably well agrees with the measured values for all feeds. The power for feed conversion was calculated as $P_c = Aj\Delta H$, where $A = 0.108 \text{ m}^2$ is the melt surface area, and j is taken from Table 4. It accounts for the evaporation of water, reaction heat, and heating of condensed products to melt temperature and evolved gases to 100°C . The wall heat losses, P_w , were calculated in the CFD model. The larger heat losses in HLW feeds are mostly caused by the

TABLE 5 Heat balance of the melter

	HLW		LAW	
	AL-19	NG-Fe2	AN-105	AZ-102
Y (kg _{glass} kg _{feed} ⁻¹)	0.347	0.390	0.485	0.490
j (kg m ⁻² day ⁻¹)	950	1650	1965	1997
j_a (kg m ⁻² day ⁻¹)	15652	16304	10806	12109
ΔH (kJ kg ⁻¹)	5919	5076	2737	3216
w	0.94	0.97	0.79	0.92
$P_{c,E}$ (kW)	7.0	10.5	6.7	8.0
$P_{c,CFD}$ (kW)	7.4	11.9	6.2	5.8
$P_{w,CFD}$ (kW)	6.8	6.6	4.4	4.3
$P_{a,E}$ (kW)	9.8	10.2	9.3	10.2
P_M (kW)	18.8	25.7	22.8	22.9
P_{CFD} (kW)	19.8	24.9	19.3	20.9

Note: Subscripts M, E, and CFD denote values measured, estimated, and calculated by the CFD model, respectively.

Abbreviations: HLW, high-level wastes; LAW, low-activity wastes.

deeper 74 cm glass pool depth of DM100-BL as opposed to 48 cm glass pool depth of DM100-WV. Finally, the heating of plenum gases can be estimated as

$$P_a = jA \left(\frac{1}{Y} - 1 \right) [wc_{p,w}\Delta T + (1-w)c_{p,g}\Delta T] + Aj_a c_{p,a} \Delta T_a \quad (19)$$

where Y is the glass yield (mass of glass per mass of feed), w is the mass fraction of water in the gases evolved from slurry feed, ΔT is the temperature increase from 100°C to melter plenum temperature, j_a is the air mass flux, ΔT_a is the air temperature increase, and $c_{p,w}$, $c_{p,g}$, and $c_{p,a}$ are the heat capacities of water vapor, dry feed gases, and air, respectively.

As nuclear waste vitrification melters are designed to operate under negative pressure, surrounding air from outside of the melter can ingress into the plenum through small leak paths in the walls and lid. Therefore, the air in melter plenum consists of bubbling air, in-leaked air, and gases evolved from the cold cap. For the purposes of the heat balance, the flux of bubbling air is negligible. The DM100 is rated for $j_a = 9067 \text{ kg m}^{-2} \text{ day}^{-1}$ of in-leaked air⁴⁸; however, based on the melter test data,^{42–45} the actual amount of in-leaked air was 20%–60% higher. The estimates of plenum space heat losses were then estimated using this higher value of j_a .

Figure 7 graphically shows the distribution of power consumption for an AN-105 feed. It demonstrates that only about 10% of the supplied power is used for dry feed conversion. The rest is consumed by water evaporation, in-leaked air heating, and heat losses through walls.

CONCLUSIONS

A CFD model of a glass melter can predict the glass production rate of a specific melter feed when augmented by a cold cap model that combines the heat transfer with the feed-to-glass conversion kinetics.

The approximate functions representing the material properties of a melter feed are designed based on experimental data from DSC, EGA, and volumetric measurements performed on feed samples heated at various heating rates. Conversion extent is based on a kinetic model based on XRD silica dissolution data.

The cold cap model resolves the spatial distribution of temperature and conversion degree within the cold cap. Therefore, it estimates the profiles of material properties, the condensed phase velocity, and the heating rate, as well as the cold cap thickness. In its simplest form, the temperature field is one-dimensional, only the reaction layer of the cold cap is considered, and the top and bottom boundaries of the reaction zone are determined by the extent of conversion.

The temperature and heat fluxes at the boundaries depend on the interaction between the cold cap and its environment. At steady state, a relationship exists between the cold cap bottom temperature and the heat fluxes to the cold cap. This enables the development of a surrogate cold cap model that facilitates the integrated cold cap–CFD model methodology.

The model was applied for melting of two HLW and two LAW simulant melter feeds with considerably different properties and predicts glass production rates that are in reasonable agreement with the reported values for a pilot-scale, Joule-heated melter. Minor discrepancies observed for moderately foaming feeds indicate that refining the experimental evaluation of cold cap properties may further improve agreement with pilot-scale data.


ACKNOWLEDGMENTS


This work was supported by the U.S. Department of Energy's Waste Treatment and Immobilization Plant Project of the Office of River Protection. Richard Pokorný, Jaroslav Kloužek, and Miroslava Vernerová acknowledge financial support from the Czech Ministry of Education, Youth and Sports Project no. LTAUSA18075. The CFD model development was performed by Battelle Energy Alliance, LLC under the U.S. Department of Energy Idaho Operations Contract DE-AC07-05ID14517. This research made use Idaho National Laboratory computing resources that are supported by the Office of Nuclear Energy of the U.S. Department of Energy and the Nuclear Science

User Facilities under Contract no. DE-AC07-05ID14517. We would like to thank Jaehun Chun for expertly reviewing and Maura Zimmerschied for meticulously editing the manuscript.

ORCID

Pavel Ferkl  <https://orcid.org/0000-0003-2844-3199>

Alexander Abboud  <https://orcid.org/0000-0001-6789-0077>

Donna Post Guillen  <https://orcid.org/0000-0002-7718-4608>

Jaroslav Kloužek  <https://orcid.org/0000-0002-6826-1632>

Richard Pokorný  <https://orcid.org/0000-0002-9023-0381>

REFERENCES

- Schill P, Chmelar J. Use of computer flow dynamics in glass technology. *J Non Cryst Solids*. 2004;345–346:771–6. <https://doi.org/10.1016/j.jnoncrsol.2004.08.199>
- Abbassi A, Khoshmanesh K. Numerical simulation and experimental analysis of an industrial glass melting furnace. *Appl Therm Eng*. 2008;28:450–9. <https://doi.org/10.1016/j.applthermaleng.2007.05.011>
- Choudhary MK, Venuturumilli R, Hyre MR. Mathematical modeling of flow and heat transfer phenomena in glass melting, delivery, and forming processes. *Int J Appl Glass Sci*. 2010;1:188–214. <https://doi.org/10.1111/j.2041-1294.2010.00018.x>
- Li H, Xing Z, Xu S, Liu S. 3D simulation of borosilicate glass all-electric melting furnaces. *J Am Ceram Soc*. 2014;97:141–9. <https://doi.org/10.1111/jace.12597>
- Zhou J, Takahashi H, Tsuzuki N, Kikura H. Investigation of flow behavior of Joule-heating flow in a 2-D model of a reprocessing glass melter cavity. *J Flow Control Meas Visual*. 2018;6:199–216. <https://doi.org/10.4236/jfcmv.2018.64016>
- Jebavá M, Hrbek L, Němec L. Energy distribution and melting efficiency in glass melting channel: effect of heat losses, average melting temperature and melting kinetics. *J Non Cryst Solids*. 2019;521:119478. <https://doi.org/10.1016/j.jnoncrsol.2019.119478>
- Suneel G, Kaushik CP, Satya Sai PM, Gayen JK, Ravi KV. Enhancement of glass production rate in Joule heated ceramic melter. *Chem Prod Process Model*. 2019;15:20190068. <https://doi.org/10.1515/cppm-2019-0068>
- Li L, Han J, Lin H, Ruan J, Wang J, Zhao X. Simulation of glass furnace with increased production by increasing fuel supply and introducing electric boosting. *Int J Appl Glass Sci*. 2020;11:170–84. <https://doi.org/10.1111/ijag.13907>
- Pokorný R, Hilliard ZJ, Dixon DR, Schweiger MJ, Guillen DP, Kruger AA, et al. One-dimensional cold cap model for melters with bubble. *J Am Ceram Soc*. 2015;98:3112–8. <https://doi.org/10.1111/jace.13775>
- Pokorný R, Kruger AA, Hrma P. Mathematical modeling of cold cap: effect of bubbling on melting rate. *Ceram Silik*. 2014;58:296–302.
- Pokorný R, Hrma P. Mathematical modeling of cold cap. *J Nucl Mater*. 2012;429:245–56. <https://doi.org/10.1016/j.jnucmat.2012.06.013>

12. Pokorny R, Hrma P. Model for the conversion of nuclear waste melter feed to glass. *J Nucl Mater.* 2014;445:190–9. <https://doi.org/10.1016/j.jnucmat.2013.11.009>
13. Hrma PR, Schweiger MJ, Humrickhouse CJ, Moody JA, Tate RM, Rainsdon TT, et al. Effect of glass-batch makeup on the melting process. *Ceram Silik.* 2010;54:193–211.
14. Ungan A, Viskanta R. Melting behavior of continuously charged loose batch blankets in glass melting furnaces. *Glastech Ber.* 1986;59:279–91.
15. Mase H, Oda K. Mathematical model of glass tank furnace with batch melting process. *J Non Cryst Solids.* 1980;38–39:807–12. [https://doi.org/10.1016/0022-3093\(80\)90536-0](https://doi.org/10.1016/0022-3093(80)90536-0)
16. Kuhn WS. Mathematical modeling of batch melting in glass tanks. In: Loch H, Krause D, editors. *Mathematical simulation in glass technology.* New York: Springer; 2002. p. 73.
17. Oda K. Mathematical modelling of batch melting process in cold-top electric furnace. *J Ceram Soc Jpn.* 2022;130:22068. <https://doi.org/10.2109/jcersj2.22068>
18. Dixon DR, Schweiger MJ, Riley BJ, Pokorny R, Hrma P. Temperature distribution within a cold cap during nuclear waste vitrification. *Environ Sci Technol.* 2015;49:8856–63. <https://doi.org/10.1021/acs.est.5b00931>
19. Ferkl P, Hrma P, Abboud A, Guillen DP, Khawand J, Kopal I, et al. Conversion kinetics during melting of simulated nuclear waste glass feeds measured by dissolution of silica. *J Non Cryst Solids.* 2022;579:121363. <https://doi.org/10.1016/j.jnoncrystol.2021.121363>
20. Pegg IL. Turning nuclear waste into glass. *Phys Today.* 2015;68:33–9. <https://doi.org/10.1063/PT.3.2687>
21. Pokorny R. Molten salt migration in the cold cap, PNNL-25068. Richland, WA: Pacific Northwest National Laboratory; 2015.
22. Hrma P, Gales CE, Yasuda DD. Drainage of primary melt in a glass batch. *Ceram Trans.* 1991;23:361–7.
23. Hrma P. Thermodynamics of batch melting. *Glastech Ber.* 1982;55:138–50.
24. Ferkl P, Hrma P, Klouček J, Vernerová M, Kruger A, Pokorný R. Model for batch-to-glass conversion: coupling the heat transfer with conversion kinetics. *J Asian Ceram Soc.* 2021;9:652–64. <https://doi.org/10.1080/21870764.2021.1907914>
25. Šesták J, Berggren G. Study of the kinetics of the mechanism of solid-state reactions at increasing temperatures. *Thermochim Acta.* 1971;3:1–12. [https://doi.org/10.1016/0040-6031\(71\)85051-7](https://doi.org/10.1016/0040-6031(71)85051-7)
26. Šesták J. Šesták–Berggren equation: now questioned but formerly celebrated—what is right. *J Therm Anal Calorim.* 2017;127:1117–23. <https://doi.org/10.1007/s10973-015-4998-x>
27. Ferziger JH, Peric M. *Computational methods for fluid dynamics.* vol.3. New York: Springer; 2002.
28. Modest MF. *Radiative heat transfer.* 2nd ed. London: Academic Press; 2003.
29. Hirt CW, Nichols BD. Volume of fluid (VOF) method for the dynamics of free boundaries. *J Comput Phys.* 1981;39:201–25. [https://doi.org/10.1016/0021-9991\(81\)90145-5](https://doi.org/10.1016/0021-9991(81)90145-5)
30. Abboud AW, Guillen DP. A methodology to reduce the computational cost of transient multiphysics simulations for waste vitrification. *Comput Chem Eng.* 2018;115:64–80. <https://doi.org/10.1016/j.compchemeng.2018.03.027>
31. Abboud AW, Guillen DP, Hrma P, Kruger AA, Klouček J, Pokorny R. Heat transfer from glass melt to cold cap: computational fluid dynamics study of cavities beneath cold cap. *Int J Appl Glass Sci.* 2021;12:233–44. <https://doi.org/10.1111/ijag.15863>
32. Siemens. User guide, Star-CCM+ Version 15.02.007-R8. 2020.
33. Guillen DP, Abboud AW, Pokorny R, Eaton WC, Dixon D, Fox K, et al. Development of a validation approach for an integrated waste glass melter model. *Nucl Technol.* 2018;203:244–60. <https://doi.org/10.1080/00295450.2018.1458559>
34. Abboud AW, Guillen DP, Pokorny R. Effect of cold cap coverage and emissivity on the plenum temperature in a pilot-scale waste vitrification melter. *Int J Appl Glass Sci.* 2020;11:357–68. <https://doi.org/10.1111/ijag.15031>
35. Guillen DP, Abboud AW, Eaton WC, Dixon D, Pokorny R, Fox K, et al. Melter modeling over a range of scales to support vitrification at the WTP. *Waste Management Symposia;* 2019. p. 13.
36. Lee S, Cutforth DA, Mar D, Klouček J, Ferkl P, Dixon DR, et al. Melting rate correlation with batch properties and melter operating conditions during conversion of nuclear waste melter feeds to glasses. *Int J Appl Glass Sci.* 2021;12:398–414. <https://doi.org/10.1111/ijag.15911>
37. Hrma P, Pokorny R, Lee S, Kruger AA. Heat transfer from glass melt to cold cap: melting rate correlation equation. *Int J Appl Glass Sci.* 2019;10:143–50. <https://doi.org/10.1111/ijag.12666>
38. Lee S, Ferkl P, Pokorny R, Klouček J, Hrma P, Eaton WC, et al. Simplified melting rate correlation for radioactive waste vitrification in electric furnaces. *J Am Ceram Soc.* 2020;103:5573–8. <https://doi.org/10.1111/jace.17281>
39. Hujova M, Pokorny R, Klouček J, Dixon DR, Cutforth DA, Lee S, et al. Determination of heat conductivity of waste glass feed and its applicability for modeling the batch-to-glass conversion. *J Am Ceram Soc.* 2017;100:5096–106. <https://doi.org/10.1111/jace.15052>
40. Pokorny R, Rice JA, Schweiger MJ, Hrma P. Determination of temperature-dependent heat conductivity and thermal diffusivity of waste glass melter feed. *J Am Ceram Soc.* 2013;96:1891–8. <https://doi.org/10.1111/jace.12313>
41. Rice JA, Pokorny R, Schweiger MJ, Hrma P. Determination of heat conductivity and thermal diffusivity of waste glass melter feed: extension to high temperatures. *J Am Ceram Soc.* 2014;97:1952–8. <https://doi.org/10.1111/jace.12971>
42. Kruger AA, Pegg IL, Chaudhuri M, Gong W, Gan H, Matlack KS, et al. Melt rate enhancement for high aluminum HLW glass formulation, VSL-08R1360-1, Rev. 0. Richland, WA (United States): Hanford Site (Wash.); 2013. <https://doi.org/10.2172/1105973>
43. Kruger AA, Gan H, Joseph I, Pegg IL, Matlack KS, Chaudhuri M, et al. Melter throughput enhancements for high-iron HLW, VSL-12R2490-1. Richland, WA (United States): Vitreous State Laboratory; 2012. <https://doi.org/10.2172/1059419>
44. Kruger AA, Muller IS, Gong W, Pegg IL, Matlack KS. DuraMelter 100 tests to support LAW glass formulation correlation development, VSL-06R6480-1, Rev. 0. Richland, WA (United States): Hanford Site (Wash.); 2013. <https://doi.org/10.2172/1109494>
45. Matlack KS, Muller IS, Gong W, Pegg IL. Small scale melter testing of LAW salt phase separation VSL-07R7480-1, Rev. 0. Richland, WA (United States): The Catholic University of

- America, Vitreous State Laboratory; 2007. <https://doi.org/10.2172/1514890>
46. Gustafson K, Abe T. The third boundary condition—was it robin's? *Math Intell.* 1998;20:63–71. <https://doi.org/10.1007/BF03024402>
47. Lee SM, Hrma P, Pokorny R, Traverso JJ, Klouzek J, Schweiger MJ, et al. Heat transfer from glass melt to cold cap: effect of heating rate. *Int J Appl Glass Sci.* 2019;10:401–13. <https://doi.org/10.1111/ijag.13104>
48. Joseph I. Private communication. 2021.

How to cite this article: Ferkl P, Hrma P, Abboud A, Guillen DP, Vernerová M, Kloužek J, et al. Conversion degree and heat transfer in the cold cap and their effect on glass production rate in an electric melter. *Int J Appl Glass Sci.* 2023;14:318–329. <https://doi.org/10.1111/ijag.16615>